STAR Note 347

Coherent Peripheral Collisions with STAR

Spencer Klein and Joakim Nystrand

Lawrence Berkeley National Laboratory
Berkeley, California 94720, U.S.A.

June 3, 1998

Abstract

The peripheral collisions program for STAR at RHIC is described. We discuss some of the physics that can be studied by observing coherent nuclear interactions, whereby the nuclei miss each other, but interact by longer ranged electromagnetic and hadronic interactions. The experimental feasibility of making these measurements with STAR is described, and we discuss the expected backgrounds along with the analysis techniques and triggering algorithms necessary to reject these backgrounds while accepting the interesting signals.

1 Introduction

The peripheral collisions program in STAR will study the interactions of the coherent electromagnetic and strong force fields carried by the colliding nuclei. Even though the nuclei may physically miss each other, these fields can interact because of their relatively long range. In these interactions, the exchange forces couple coherently to the entire nuclei, and the nuclei remain intact or nearly intact.

These interactions include two–photon interactions, γ–Pomeron and possibly Pomeron–Pomeron interactions. RHIC[1] will be the first accelerator to reach energies high enough for these processes to be studied via coherently coupling heavy nuclei. Previously, two–photon interactions have been studied at e^+e^- accelerators. Photon-Pomeron interactions have been studied with low energy photons beams, with proton targets at HERA, and with nuclear targets by E-665 at Fermilab and the NMC collaboration at CERN.

This STAR Note will summarize the current status of the peripheral collisions program in STAR. The two–photon luminosity, RHIC production rates and early background estimates were discussed previously in STAR Note 243[2]. Here, we update that work and present new results on γ–Pomeron interactions and GEANT based simulations of two-photon events from STARLight.

Final State	$\Gamma_{\gamma\gamma}$	Au+Au		I+I		O+O	
	[keV]	σ [μb]	Evts./Year	σ [μb]	Evts./Year	σ [μb]	Evts./Year
π^0	7.8 eV	4700	$9.5 \cdot 10^6$	1100	$3.0 \cdot 10^7$	1.1	$1.1 \cdot 10^6$
η	0.5	920	$1.8 \cdot 10^6$	240	$6.4 \cdot 10^6$	0.32	$3.1 \cdot 10^5$
η'	4.3	660	$1.3 \cdot 10^6$	180	$4.9 \cdot 10^6$	0.30	$3.0 \cdot 10^5$
$f_0(980)$	0.6	110	$2.2 \cdot 10^5$	31	$8.3 \cdot 10^5$	0.052	$5.1 \cdot 10^4$
$f_2(1270)$	2.8	540	$1.1 \cdot 10^6$	160	$4.2 \cdot 10^6$	0.30	$2.9 \cdot 10^5$
$a_2(1320)$	1.0	170	$3.4 \cdot 10^5$	49	$1.3 \cdot 10^6$	0.10	$9.5 \cdot 10^4$
$f_2'(1525)$	0.1	8	$1.5 \cdot 10^4$	2	$6.2 \cdot 10^4$	0.005	$4.9 \cdot 10^3$
$\pi_2(1670)$	1.4	64	$1.3 \cdot 10^5$	20	$5.3 \cdot 10^5$	0.045	$4.4 \cdot 10^4$
$\eta_c(2980)$	7.5	2.6	$5.2 \cdot 10^3$	0.92	$2.5 \cdot 10^4$	0.004	$3.4 \cdot 10^3$
$\mu^+\mu^-$	–	130 mb	$2.7 \cdot 10^8$	34 mb	$9.1 \cdot 10^8$	40	$3.9 \cdot 10^7$
$\tau^+\tau^-$	–	0.74	$1.5 \cdot 10^3$	0.33	$9.0 \cdot 10^3$	2.5 nb	$2.4 \cdot 10^3$
$\rho^0\rho^0$	–	21	$4.3 \cdot 10^4$	6.4	$1.7 \cdot 10^5$	14 nb	$1.4 \cdot 10^4$

Table 1: Cross sections and production rates at RHIC for various final states in two–photon interactions. The calculations are discussed in Section 3.1.

2 Physics Interests

2.1 Two–Photon Interactions

Heavy–ion accelerators offer an advantage over e^+e^- for two–photon processes since the flux of virtual photons scale as Z^2 and the interaction rate scales as the flux squared, i.e. as Z^4. The virtual photon energy spectrum has a $1/E_\gamma$ dependence up to a maximum E_γ of $\gamma\hbar c/R$. At RHIC the maximum $\gamma\gamma$ center–of–mass mass energy is thus 6 GeV for gold–gold interactions.

A wide variety of physics topics can be studied in two–photon interactions. Two photons couple to any state with internal charge constituents (i.e. quarks) and spin/parity $J^{PC} = 0^{-+}, 0^{++}, 2^{-+}$ or 2^{++} (for $J \leq 2$). The spin 0 or 2 selection is because the massless, real photon spins can be aligned or antialigned.

Possible final states can include single mesons, meson pairs, baryon pairs, lepton pairs or jets. We will discuss some of the interesting final states below, including possible strong field QED effects.

The rates for a number of final states of interest are given in Table 1. These numbers will be discussed more in the following sections.

- Meson Spectroscopy: Search for glueballs and Other Exotica

  Two-photon interactions are a very powerful tool for meson spectroscopy. Because two photons couple to (charge)^4 (because there are two photons), the two-photon width $\Gamma_{\gamma\gamma}$ is a rather direct measurement of the quark and isospin content of a mesonic final state, with

$$\sigma(\gamma\gamma \to X) = 8\pi^2(2J+1)\frac{\Gamma_{\gamma\gamma}}{2M^2}\delta(W_{\gamma\gamma} - M) \qquad (1)$$

Quark State	$Relative \Gamma_{\gamma\gamma}$	$J^{PC} = 2^{++}$ Meson	$\Gamma_{\gamma\gamma}$ (for $J^{PC} = 2^{++}$)
$\frac{\|u\overline{u}+d\overline{d}>}{\sqrt{2}}$	25	$f_2(1270)$	2.8 keV
$\frac{\|u\overline{u}-d\overline{d}>}{\sqrt{2}}$	9	$a_2(1320)$	1.0 keV
$\|s\overline{s}>$	2	$f_2'(1525)$	0.1 keV

Table 2: Relative $\gamma\gamma$ coupling and cross sections for different states.

where J is the spin and M the mass of the final state X. For non-$q\overline{q}$ states, the coupling will be different, with lower coupling predicted for objects like four-quark states ($q\overline{q}q\overline{q}$), hybrids ($q\overline{q}g$) and glueballs (states composed totally or largely of gluons). As Table 2 shows, for well understood mesons, the data agrees rather well with the predictions.

Mesons spectroscopy is of interest because there is good evidence of the existence of at least some exotic (non $q\overline{q}$) states. SU(3) predicts the number of mesons with specified spins and isospins. Although exact calculations are difficult for light quarks, the masses and transition of these states can be roughly predicted with few complications. However, in the range 0.8 to 2.5 GeV, experiments have found quite a few more states than fit into SU(3).

Here, we give two examples. The $\xi(2230)$, also known as the $f_J(2230)$ decays to $K\overline{K}$ (both charged and neutral). It has been observed by the Mark III and BES collaborations in radiative J/ψ decays, a mode believed mediated by two gluons. It has also been observed in πp interactions. However, it has not been seen in $\gamma\gamma$ interactions. The relative coupling is given by a quantity called 'stickiness', $S = \Gamma(gg)/\Gamma(\gamma\gamma)$; the relative coupling of a state to gluons compared with photons. Stickiness is normalized to 1 for the $f_2(1270)$, a well accepted $q\overline{q}$ meson. For the $\xi(2230)$, the CLEO collaboration found that $S > 76$ at a 95% confidence level[3]. This seems too large for a $q\overline{q}$ meson. For this reason, the $\xi(2230)$ is now considered to be a fairly good glueball candidate.

The $f_0(980)$ is another example. A normal $q\overline{q}$ meson with this mass and spin would have $\Gamma_{\gamma\gamma} \sim 2.5$ keV. However, experimentally $\Gamma_{\gamma\gamma} = 0.6 \pm 0.1$ keV. This discrepancy seems too large to be explained by minor factors. However, unlike the $\xi(2230)$, there is no agreement on the nature of the $f_0(980)$; one way to explain the coupling is if it is a $K\overline{K}$ molecule, two kaons bound together[4].

- Meson form factors (pairs)

  Two photon interactions also produce meson (or lepton) pairs via $\gamma\gamma \rightarrow X\overline{X}$. Although this is a simple reaction, it has a rather complex underbody, with several mechanisms coming into play.

  Most simply, meson production follows Fig. 1(a). At the hadron level, photons couple only to charged mesons. So, $\pi^+\pi^-$ should be produced, but not $\pi^0\pi^0$. This picture applies near threshold, where the photon wavelength is large compared to the size

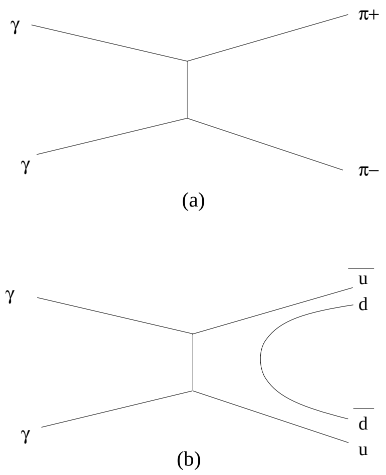

Figure 1: Meson Production via (a) hadronic couplings or via (b) quark couplings.

of the meson. However, at higher energies, the photons 'see' and couple to quarks, as in Fig. 1(b) and both $\pi^+\pi^-$ and $\pi^0\pi^0$ are produced in comparable numbers. By comparing the rates of the two final states, the transition can be studied, and the size of the mesons determined.

However, for some channels, other mechanisms may apply. The reaction $\gamma\gamma \rightarrow \rho^0\rho^0$ is of special interest. A resonance is observed near threshold, for $M_{\rho\rho} \sim 1.3 - 1.6$ GeV. A similar resonance is not observed in the $\rho^+\rho^-$ channel. To quote the particle data book, "This process has not been explained by models in which only conventional resonances dominate[4]." Four quark interpretations are popular[5], but are by no means the only interpretation.

At higher energies, vector meson pairs are expected to be produced dominantly by vector meson dominance. The two photons both fluctuate into $q\overline{q}$ pairs, which then interact by elastic scattering (Pomeron exchange), becoming real[6]. These interactions are a strong test of factorization for the Pomeron:

$$\frac{d\sigma(\gamma p \rightarrow V_1 p)}{dt} \; \frac{d\sigma(\gamma p \rightarrow V_2 p)}{dt} = \frac{d\sigma(\gamma\gamma \rightarrow V_1 V_2)}{dt} \; \frac{d\sigma(pp \rightarrow pp)}{dt} \tag{2}$$

where t is the momentum transfer between the two particles. Above the threshold region, all of these processes should vary slowly with energy. Experimentally, these processes may be confused with double $\gamma P \rightarrow V$ reactions by a single ion pair. Study is required to determine if the two processes can be separated. These relations are only expected to hold when the energies are high enough that meson exchange effects are small. Although RHIC will reach these photon energies, the rates may be small. Stan Brodsky has also suggested looking for $\gamma\gamma \rightarrow \pi^0\pi^0$ where the photons fluctuate into π^0s which then become real by exchanging an Odderon[7].

Pair production by two photons has been studied at PEP and PETRA for charged and neutral pions, charged kaons, and, with limited statistics, for neutral kaons, K^* and

ρ pairs[8]; RHIC will be able to study many of these states with improved statistics, and, more importantly, extend the study to a variety of other mesons. For $\rho^0\rho^0$ in particular, more statistics are needed to clarify the shape of the resonance.

- Baryon pairs

  Two-photon interactions can also produce baryon pairs. The rates for baryon production are quite high. The rates cannot be explained simply in a coalescence model which requires three independently produced quarks to meet and unite. However, models in which a diquark (semi- bound state of two quarks) anti-diquark pair are pulled from the vacuum, and joined with a single quark-antiquark pair can explain the data. Diquark models are also required to explain the production of baryons in single photon e^+e^- annihilation[9]. A diquark calculation has been found to match the data for production of $p\overline{p}$ and $\Lambda\overline{\Lambda}$ pairs[10]. RHIC will be able to extend this study to other baryon pairs as well. Of particular interest will be the study of radially excited baryons.

  Beyond this, the production of clean baryon-antibaryon states may offer unique opportunities for baryon spectroscopy.

- QED Topics and τ pairs

  Because $Z\alpha \sim 0.6$ is large, interesting QED effects should be present at RHIC. The cross section for processes like $AuAu \rightarrow AuAue^+e^-$ is huge, about 30,000 barns, and there is considerable difference between different calculations.

  Because the fields are so strong, the colliding electromagnetic fields cannot be represented as single photons; if the fields are quantized into photons, each field contributes 1 to n photons, and the calculations become difficult[11], requiring CPU intensive solutions to the Dirac equation via the coupled channel formalism.

  Recently, Baltz and McLerran [12] completed an exact calculation of pair production, and found a cross section much lower than the coupled channel results, and very close to the perturbative result.

  One clear manifestation of the strong fields is that, at small impact parameter, the cross section violates unitarity with $d\sigma db > 2\pi bdb$. So, several pairs will be produced in each collision[13].

  Because STAR is sensitive only to charged particles with $p_\perp \gg m_e$, we will observe only the high $p_\perp$ (and hence pair mass) tail of the spectrum. Although possibly less interesting than the whole spectrum, there is still good physics. One of our first analyses will be to look at the e^+e^- spectrum, to see if perturbative (and any other) calculations hold up. With slightly more data (< 1 year), we should have good statistics on multiple pairs, and, also multiple reactions from a single collision, such as $\gamma\gamma \rightarrow e^+e^-$ from the same gold pair that also produces $\gamma P \rightarrow V$ (discussed in the next section). These reactions can be separated from multiple independent interactions in the same crossing by requiring all of the particles to come from a single vertex.

Strong field effects may manifest themselves in non-Poissonian behavior of the multiple interactions.

RHIC will also produce about 1,500 tau pairs per year with gold beams (for Iodine the expected number is about 9,000). Although the rate is fairly low, there will be no background from the process $e^+e^- \rightarrow l^+l^-$ as is seen at e^+e^- colliders; to date there are only two measurements(one titled 'evidence for...') of tau production in two-photon interactions[14]. STAR could study this reaction in some detail, and study the correlation between the τ decay angular distributions[2] between the angular decays.

2.2 γ–Pomeron Interactions

Despite many years of study, the nature of the Pomeron is unclear[15]. There is agreement that Pomerons carry the strong force but are colorless, and that they have the quantum numbers of the vacuum, $J^P = 0^{++}$. Beyond that, there is disagreement. They are often divided into two classes, soft Pomerons, which apply at low Q^2, and hard Pomerons, which apply at high Q^2. However, the dividing line is fuzzy, and they may or may not be the same object.

The soft Pomeron represents the absorptive part of the nuclear cross section. For γP interactions, the photon can be considered as a Foch state consisting of a bare photon plus various $q\overline{q}$ fluctuations. When the nucleus absorbs some of the photon wave function, a $q\overline{q}$ pair may become dominant. This pair can then elastically scatter off of the nucleus and emerge as a real vector meson. The angular distribution matches a plane wave scattering from a black disc. This picture accurately describes a large number of reactions, among them pp elastic scattering, high energy γp interactions at HERA[16] and μN interactions at Fermilab experiment E-665[17] and NMC[18]. It properly predicts the transverse momentum distribution, including the diffraction minima.

The hard Pomeron is usually treated as a state consting of two or more gluons. Two popular variants of this are Donnachie-Landschoff Pomerons, where the gluons are given structure functions, and the BFKL Pomeron, which is an infinite gluon ladder. The hard gluon is often used to describe hard interactions, such as jets (or Ws) accompanied by rapidity gaps characteristic of colorless interactions that have been observed at the Fermilab collider and elsewhere. There is as yet no clear connection between hard and soft Pomerons.

Photon-Pomeron interactions at RHIC is best described by the soft Pomeron paradigm. STAR will study physics similar to E-665 and NMC, but with greatly improved statistics, photon energy range, and final state resolution. All three of these factors allow a vast range of new physics studies. Because the high rates enter into the new physics possibilities, we list them here before discussing the rate calculations. For gold at the RHIC design luminosity, the ρ^0 production rate is 28 Hz, while the ω rate is 3 Hz, and ϕ are produced at 1 Hz. An additional term, due to meson exchange, will further increase these rates.

These rates will be ample for exploring the production reaction, measuring the Pomeron-nucleon coupling, measuring the $\rho, \omega \rightarrow \pi^+\pi^-$ lineshape, including the ρ - ω interference term. STAR can also determine if the nucleus breaks up after Pomeron emission. In the simple, absorptive model, the nucleus should be undisturbed.

The high rates also allow studies of strong field QED. At grazing incidence ($b = 2R$), a gold on gold collision has about an 0.5% chance of coherently photoproducing a ρ. Thus, the rate for multiple interactions producing multiple vector mesons is significant. If the incoming EM field is really a number of virtual photons, then the number of mesons produced should be calculable based on a Poisson distribution. However, if the incoming field is coherent, non-Poissonian variations may be seen, a good sign of strong field QED.

Calculations discussed below, predict that RHIC should produce 21,000 J/ψ per year. However, for J/ψ, the soft Pomeron calculation may break down. The soft Pomeron predicts that $\sigma \sim W^\alpha$, where W is the photon–nucleon center–of–mass energy, and the $\alpha \sim 0.22$ is characteristic of the soft Pomeron. However, for J/ψ at HERA, $\alpha \sim 0.8$. This may signal the failure of the soft Pomeron model, or be due to threshold effects[16]. RHIC can shed light on this by examining how the rate scales with k and A, the nuclear size.

STAR can also search sensitively for excited ρ and ϕ states, such as the $\rho(1450)$, $\rho(1700)$, $\omega(1600)$, $\phi(1680)$. There is little data on these states; STAR can both provide spectroscopic and decay information, and test their coupling to the nucleus.

Besides the final state reconstruction, γP interactions can be separated from $\gamma\gamma$ interactions on the basis of their final state rapidity distributions. Photons couple to nuclei as $1/k$, while Pomerons coupling is independent of Pomeron energy (one reason that it doesn't make sense to treat the Pomeron as a real particle). Because of this, γP interactions cover a wider rapidity range than $\gamma\gamma$, and the photon 'direction' can be statistically determined.

2.3 Pomeron–Pomeron Interactions

Coherent double Pomeron interactions are also possible. Because of the short range of the Pomeron, this is only possible for a rather narrow range of impact parameters: $2R + 2\Delta > b > 2R$, where Δ is the 'range' of the Pomeron. Unfortunately, there are few calculations of double Pomeron rates in heavy ion collisions. A calculation, of Higgs production from PP, found that the production cross section was independent of A[19]. A calculation of η_c and η_b production rates using the same approach found that for heavy nuclei the PP rates are negligible compared to those from $\gamma\gamma$[20].

These calculations can be criticized because of their use of an Gaussian form factor for the nucleus which is inaccurate for $b > R_N$. The use of a more accurate form factor might lead to a cross section that rises as $A^{1/3}$. This does not appear sufficient to change the conclusions about the relative sizes of PP and $\gamma\gamma$ rates.

There is very limited data about this subject. The only data on PP interactions with nuclei comes from colliding α particles at the ISR. The PP cross section for $\alpha\alpha$ was about 11 times that for *pp*, a similar A dependence as the total cross section, so that, in both cases, PP interactions were about 0.2% of the total cross section[21]. Of course, α particles are light enough that scaling with A is not expected. However, if these results hold up for heavier nuclei, then the PP cross section could be significant.

Whatever the case for gold on gold collisions, $\gamma\gamma$ and γP interactions will dominate. For *pp*, it seems clear that PP interactions dominate. So, as A varies, the relative strength of the

Pomeron and photon components of the interaction will vary, providing clear measurements of the overall strength of the Pomeron interactions. One interesting challenge will be to find the cleanest final state for PP interactions, to best measure their strength.

It is difficult to explain double Pomeron collisions in the soft Pomeron model; at least some aspects of the hard Pomeron are needed. Because of the great uncertainties in PP cross sections, they are unlikely to be a major part of the STAR Year 1 physics program. For these reasons, we do not consider them further here.

2.4 Interference Signals

All of these interactions begin with an identical final state: two heavy ions. Many final states can be produced via more than one intermediate mechanism. This opens up the possibility of interference. This is likely to develop into one of the most interesting topics in peripheral collisions.

One clear case of interference is between $\gamma\gamma \rightarrow e^+e^-$ and $\gamma P \rightarrow V \rightarrow e^+e^-$, where V is a vector meson. Because the $\gamma\gamma$ and γP states have opposite C parity, the interference final state must be asymmetric in the exchange of the electron and positron momenta. Several early experiments studied interference for ρ, ω and ϕ mesons[22, 23]. The experimenters used a low energy photon beam incident on light (beryllium or carbon) targets, and measured the number of events where the electron had a higher momentum than the positron, as a function of final state invariant mass. For light targets, where final state meson-nucleus interactions are expected to be small, the interference angle is a measure of the production phase of the meson. For the ρ, these results included a large single pion exchange component.

STAR will use heavy nuclei as targets, so the interference angle will also include a large term due to final state vector meson-nucleus interactions. We will be able to extract σ_{VN} from this measurement. This will be of particular interest for the J/ψ, because of the apparent large $\sigma_{J/\psi N}$ observed by NA-50[24].

STAR will be able to observe interference because, in most photonuclear events, the photon energy will be less than the Pomeron energy (because $N_\gamma \sim 1/k$, while $N_P \sim 1$). STAR will observe an asymmetry in the number of events where the electron has a higher energy times the final state rapidity, with center ($y = 0$) events having no asymmetry.

Because of the greatly increased acceptance, final state resolution and data rate, STAR will also be able to look at many more variables than these early experiments. Of particular interest will be our ability to measure asymmetries as function of photon energy (related to y), total final state $p_\perp$ (coherent vs. incoherent events), and decay angles.

Of at least comparable interest, STAR should also be able to look at a variety of other interference channels. One very interesting possibility would be $\gamma\gamma \rightarrow \pi^+\pi^-$ and $\gamma P \rightarrow \rho^0 \rightarrow \pi^+\pi^-$. Although the rate for the ρ channel is vastly higher than for the $\gamma\gamma$ channel, by selecting events close to the beam, and looking at on the sides of the ρ^0 mass peak, interference may be observable. A similar possibility may occur for $\gamma\gamma \rightarrow K^+K^-$ and $\gamma P \rightarrow \phi \rightarrow K^+K^-$.

2.5 Other Topics – Pion Fields

Many other topics can be studied with peripheral collisions. We mention here only one recent example: collision and consequent excitation of the nuclear pions fields to produce a DCC[25]. This process may be aided by the strong electromagnetic field, which will tip the 'Mexican Hat,' enhancing DCC production[26].

Besides a Pomeron field, nuclei are also surrounded by meson fields, with pion fields the major component. In collisions in a narrow range of impact parameters, the nuclei may miss each other, but the pion fields may collide. When this happens, the fields may become excited, equivalent to a vacuum excitation. When this excitation decays away, a DCC may be formed. This DCC would most likely manifest itself as a cloud of $\gamma = 100$ pions traveling down the beampipe, with a charged: neutral pion distribution that of a DCC. Rates for this process remain to be determined.

3 Luminosity and Production Rates

3.1 Two–Photon Interactions

The two–photon luminosity in high–energy nuclear collisions can be calculated by the Weizsäcker–Williams method [28, 29, 30]. In this method, the electromagnetic field of a nucleus is treated as a pulse of real ($Q^2 = 0$) photons. The photon energies extend up to a maximum energy of $\sim \gamma\hbar c/R$, about 3 GeV for gold at RHIC.

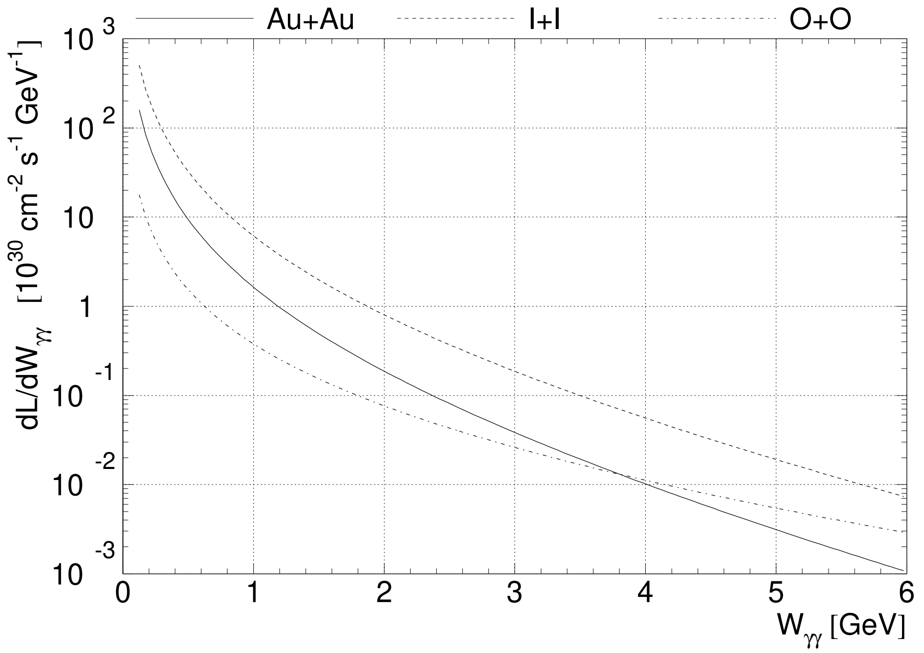

Figure 2: Two–Photon luminosity for 3 different nuclear systems at RHIC.

Quantitatively, the intensity of the equivalent radiation is calculated, in the Weizsäcker–Williams method, from the Fourier transformation of the Poynting vector of the electromagnetic field. The electromagnetic field of a nucleus in a non–disruptive ($b > R_1 + R_2$) collision is, by virtue of Gauss' theorem, equivalent to that of a point charge. The corresponding radiation density at an impact parameter b is given by [31]:

$$n(E_\gamma, b) = \frac{dN}{dE_\gamma d^2b} = \frac{Z^2\alpha}{\pi^2}\frac{1}{\beta^2}\frac{1}{E_\gamma b^2}x^2\left\{K_1^2(x) + \frac{1}{\gamma^2}K_0^2(x)\right\} \tag{3}$$

where $x = bE_\gamma/\beta\gamma$ and E_γ is the photon energy. $K_0(x)$ and $K_1(x)$ are modified Bessel functions. In Eq. 3 and throughout natural units are used, i.e. $\hbar = c = 1$.

The equivalent two–photon luminosity is given as the product of the nuclear luminosity with the photon densities of the two nuclei, integrated over impact parameter. The calculation for nucleus–nucleus collisions is complicated by the fact that when the nuclear impact parameter b is smaller than sum of the nuclear radii, hadronic (strong) interactions are likely to dominate. This region must therefore be excluded. The differential two–photon luminosity is given by:

$$\frac{d\mathcal{L}_{\gamma\gamma}}{dE_1 dE_2} = \mathcal{L}_{AA}\int_{b_1>R}\int_{b_2>R} n(E_1,b_1)n(E_2,b_2)\Theta(\mid \vec{b}_1 - \vec{b}_2 \mid -2R)d^2b_1d^2b_2 \tag{4}$$

The Θ–function eliminates the contribution from the nuclear overlap. Since $n(E_\gamma, b)$ is proportional to Z^2, the luminosity essentially scales as Z^4. (The scaling is not exact because of the Θ-function and the variation of R with A/Z.)

The Θ–function in Eq. 4 implies that the nuclei have sharp edges. A more realistic model treats the nuclear density with a Wood–Saxon distribution. This will reduce the effective luminosity by about 5-30%, depending on the invariant mass[27]. Furthermore, Eq. 4 does not include interactions which occur inside one of the nuclei. Because only the charge inside a radius R corresponding to the production point will contribute to the interaction, the field strength will be reduced, and the $p_\perp$ increased; these interactions remain to be studied.

Defining a function $F(E_1, E_2)$,

$$F(E_1,E_2) = \int_{b_1>R}\int_{b_2>R} n(E_1,b_1)n(E_2,b_2)\Theta(\mid \vec{b}_1 - \vec{b}_2 \mid -2R)d^2b_1d^2b_2 \tag{5}$$

it can be shown that

$$F(E_1,E_2) = f(E_1)f(E_2) - \Delta F(E_1,E_2) \tag{6}$$

where $f(E_\gamma)$ is the photon flux of a single source integrated over impact parameter from R to ∞, and $\Delta F(E_1, E_2)$ appears because of the exclusion of the nuclear overlap [28]. $f(E)$ can be expressed analytically [31]:

$$f(E_\gamma) = \frac{2Z^2\alpha}{\pi}\frac{1}{E_\gamma}\left\{xK_0(x)K_1(x) - \frac{1}{2}x^2\left(K_1^2(x) - K_0^2(x)\right)\right\} \tag{7}$$

where $x = 2RE_\gamma/\beta\gamma$ and $\Delta F(E_1, E_2)$ is given by the two–dimensional integral:

$$\Delta F(E_1,E_2) = 4\pi\int_{b_1=R}^{\infty}\int_{b_2=max(R,b_1-2R)}^{b_1+2R} n(E_1,b_1)n(E_2,b_2)\arccos(\frac{b_1^2+b_2^2-4R^2}{2b_1b_2})b_1db_1b_2db_2 \tag{8}$$

This integral must be evaluated numerically.

It is convenient to convert from the individual photon energies E_1 and E_2 to the $\gamma\gamma$ center–of–mass energy, W, and rapidity, Y:

$$\begin{array}{rclcrcl} E_1 & = & \frac{1}{2}We^{Y} & \qquad & W & = & \sqrt{4E_1E_2} \\ E_2 & = & \frac{1}{2}We^{-Y} & \qquad & Y & = & \frac{1}{2}\ln(E_1/E_2) \end{array} \tag{9}$$

Since $F(E_1,E_2)$ is a differential quantity, $F \propto d\mathcal{L}/dE_1dE_2$, the corresponding function in the new (W,Y) coordinate system is [1]:

$$\tilde{F}(W,Y) = \frac{W}{2}F(\frac{1}{2}We^{Y},\frac{1}{2}We^{-Y}) \tag{10}$$

The tilde will be dropped from $F(W,Y)$ henceforth. The differential $\gamma\gamma$ luminosity $d\mathcal{L}_{\gamma\gamma}/dW$ is then

$$\frac{d\mathcal{L}}{dW} = \mathcal{L}_{AA}\int_{-\infty}^{\infty} F(W,Y)dY \tag{11}$$

Figure 2 shows $d\mathcal{L}_{\gamma\gamma}/dW$ at RHIC for 3 different ions. The highest luminosity occurs in I+I interactions. The lower Z for iodine compared to gold is compensated by higher nuclear luminosity and smaller radius.

It is of interest to compare the two–photon luminosities at RHIC with the corresponding luminosities at e^+e^- colliders. An expression for the latter (in the limit of $q_{1,2} \to 0$) is given by Low's formula[32, 33]:

$$\frac{d\mathcal{L}_{\gamma\gamma}}{dW} = \frac{W}{s}\left(\frac{\alpha}{\pi}\ln(\frac{s}{4m_e^2})\right)^2 \frac{1}{\tau}\left[\frac{1}{2}(2+\tau)^2\ln(\frac{1}{\tau}) - (1-\tau)(3+\tau)\right] \tag{12}$$

where $\sqrt{s}$ is the e^+e^- CM energy, W the $\gamma\gamma$ CM energy, and $\tau = W^2/s$.

Comparisons have been made with the existing accelerators LEP II (CERN) and CESR (Cornell), where the following center–of–mass energies and luminosities have been used:

$$\begin{array}{lll} \text{LEP II} & \sqrt{s} = 180\ \text{GeV} & \mathcal{L} = 5.0\cdot 10^{31}\ \text{cm}^{-2}\ \text{s}^{-1} \\ \text{CESR} & \sqrt{s} = 10\ \text{GeV} & \mathcal{L} = 2.9\cdot 10^{32}\ \text{cm}^{-2}\ \text{s}^{-1} \end{array}$$

The absence of an impact parameter cut–off in e^+e^- collisions means that the $\gamma\gamma$ system is spread over a larger interval in rapidity than is the case for heavy–ions. The luminosity for two–photon events leading to detectable final states is hence reduced. A restriction on the $\gamma\gamma$ rapidity of

$$|\sinh(Y_{\gamma\gamma})| \leq 1.0 \tag{13}$$

is frequently used to define the "useful" $\gamma\gamma$ luminosity[30, 34]. This restriction reduces the luminosity by approximately

$$\frac{Y^{(MAX)}}{\ln(\sqrt{s}/W)}\frac{d\mathcal{L}_0}{dW} \tag{14}$$

[1]Note that $\frac{W}{2}F(E_1,E_2) = \frac{2}{W}(E_1E_2F(E_1,E_2))$ where $(E_1E_2F(E_1,E_2))$ is dimensionless. Some authors define F this way.

The two–photon luminosities calculated with this restriction is shown in Fig. 3 for LEP, CESR and I+I reactions at RHIC. The luminosity for iodine at RHIC is higher than both the LEP and CESR luminosities up to a center–of–mass energy of about 2 GeV.

The luminosities in Fig. 2 can be combined with the $\gamma\gamma$ fusion cross section to calculate the production rate for various final states. For the production of a single resonance with mass M_R, spin J, width Γ and two–photon width $\Gamma_{\gamma\gamma}$ the relativistic Breit–Wigner cross section is[35]:

$$\sigma_{\gamma\gamma}(W) = 8\pi(2J+1)\frac{\Gamma_{\gamma\gamma}\Gamma}{(W^2-m_R^2)^2+\Gamma^2 m_R^2} \approx 8\pi^2(2J+1)\frac{\Gamma_{\gamma\gamma}}{2m_R^2}\delta(W-m_R) \tag{15}$$

The Breit–Wheeler formula gives the corresponding cross section for lepton pairs[36]:

$$\sigma(\gamma\gamma\rightarrow l^+l^-) = \frac{4\pi\alpha^2}{W^2}\left[\left(2+\frac{8M^2}{W^2}-\frac{16M^4}{W^4}\right)\ln\frac{W+\sqrt{W^2-4M^2}}{2M} - \sqrt{1-\frac{4M^2}{W^2}}\left(1+\frac{4M^2}{W^2}\right)\right] \tag{16}$$

where M is the lepton mass.

The cross section for the reaction $A+A\rightarrow A+A+X$ is calculated by convoluting the $\gamma\gamma$ cross sections with $F(W,Y)$:

$$\sigma(A+A\rightarrow A+A+R) = \int\int F(W,Y)\sigma_{\gamma\gamma}(W)dWdY \tag{17}$$

The cross sections and production rates for various final states are shown in Table 1. One year is taken to be 10^7 s. The cross section for ρ–pair production has been taken from experimental data (σ=96 nb)[37]. For most well established mesons in the mass range 0–2 GeV, the production rates will be between 10^5–10^7 mesons per year for Au+Au and I+I interactions.

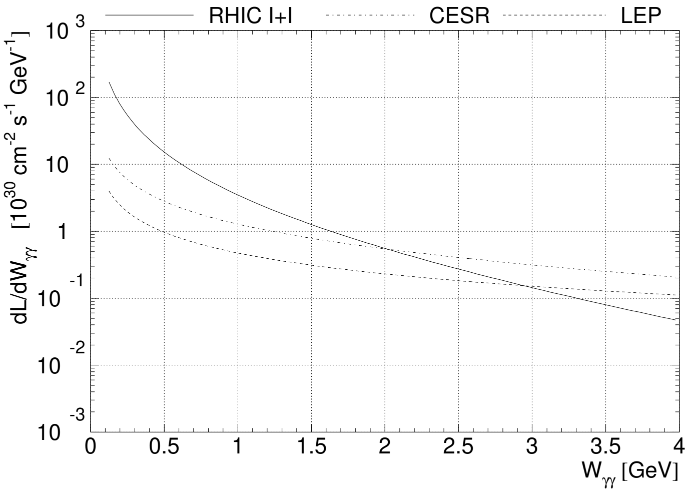

Figure 3: Comparison of the useful (see text for definition) two–photon luminosity at RHIC with the corresponding luminosity at lepton colliders.

Meson	σ_0 [μb]	k	A_V^0 [μb/GeV^2]	b [GeV^{-2}]
ρ^0	5.0	0.22	55	11
ω	0.55	0.22	5.5	10
ϕ	0.34	0.22	2.4	7
J/ψ	0.0015	0.80	0.006	4

Table 3: Parameters for the energy and t dependence of vector meson production in γp reactions.

3.2 γ–Pomeron Interactions

Since the exact nature of the Pomeron is not known, γ–Pomeron rates cannot be calculated from first principles. Instead, we present a rate calculation based on reasonable extrapolations from the vector meson production rates measured in γp interactions at HERA[16]. These results are usually interpreted within the vector dominance model where the photon fluctuates into a virtual vector meson which becomes real by elastically scattering off the proton. The elastic scattering is assumed to be mediated by an exchange particle, the soft Pomeron.

The cross section for vector meson production increases slowly with increasing γp center–of–mass energy, $W_{\gamma p}$:

$$\sigma_{\gamma p\rightarrow Vp}(W_{\gamma p}) = \sigma_0\ W_{\gamma p}^k \tag{18}$$

where k is a constant. For the light vector mesons (ρ,ω,ϕ) $k \approx 0.22$ (W in GeV), in agreement with predictions from Regge theory. For the J/Ψ, data show a stronger dependence on energy, $k \approx 0.80$. This has been interpreted as both threshold effects and as the breakdown of the soft Pomeron. At low energies, the cross sections for ρ and ω production contain an additional term due to meson exchange, which is not considered here. The values of σ_0 and k are shown in Table 3. To extrapolate this to heavy nuclei, we make the following assumptions:

1. The vertices factorize; the $\mathcal{P}p$ or $\mathcal{P}$nucleus vertex is independent of the $\gamma\mathcal{P}$ vertex.

2. The Pomeron couples coherently to the entire nucleus, as observed by E665 and NMC. The $\mathcal{P}$-nucleus coupling scales with the nuclear surface area, following the optical black disc model. In particle language, the Pomeron couples to all of the nucleons in the nucleus. However, destructive interference eliminates the contributions of the interior nucleons. The overall coupling is $A^{2/3}$, so the cross section scales as $A^{4/3}$.

3. The t dependence of the γP cross section can be interpreted as a proton form factor. If part of the t dependence comes from the Pomeron, this will be a small correction.

Because of the nuclear form factor, it is necessary to consider the momentum transfer $\sqrt{t}$ between the proton (or nucleus) and the photon. The cross section for $\gamma p \rightarrow Vp$ can be

Meson	σ [mb]	Prod. Rate [Hz]
ρ^0	69	28
ω	6.8	2.7
ϕ	2.3	0.9
J/Ψ	5.3 μb	$2.1 \cdot 10^{-3}$

Table 4: Cross sections and production rates for vector mesons in reactions of the type Au+Au $\rightarrow$ Au+Au+V.

given as

$$\sigma = \int_{t_{min}}^{\infty} dt \frac{d\sigma}{dt} = \int_{t_{min}}^{\infty} dt A_V \exp(-b|t| + c|t|^2) \tag{19}$$

where A_V, b and c depend on the final state vector meson[38, 39]. For simplicity, and with a slight loss of accuracy, we take $c = 0$. The energy dependence of the total cross section is taken into account through A_V:

$$A_V = b\sigma_0 W^k \equiv A_V^0 W^k \tag{20}$$

The values of A_V^0 and b are given in Table 3[38, 39].

The γNucleus cross section is obtained with a similar equation, but with a nuclear form factor:

$$\sigma_{\gamma A \rightarrow VA} = \int_{t_{min}}^{\infty} dt\ A^{4/3}\ A_V\ \ | F(t) |^2 \tag{21}$$

The form factor is calculated as the Fourier transformation of the nuclear charge density and can be approximated with

$$| F(t) |^2 = e^{-|t|/Q_0^2}. \tag{22}$$

with $Q_0 = 60$ MeV for Au[40]. The minimum momentum transfer is $t_{min} = [M_V^2/4E_\gamma]^2$. Since Q_0 scales as $1/R_N$, and hence as $A^{-1/3}$, the form factor reduces the overall A dependence to $A^{2/3}$.

With this, the cross section for the reaction $A + A \rightarrow A + A + V$ is given by:

$$\sigma(A + A \rightarrow A + A + V) = \int \sigma_{\gamma A \rightarrow VA} \frac{dn_\gamma}{dE_\gamma} dE_\gamma \tag{23}$$

The photon flux, dn/dE_γ can be calculated by the Weizsäcker–Williams method. In the model, it is calculated as the average flux from the emitter nucleus over the projected surface of the target nucleus, i.e.

$$\frac{dn_\gamma}{dE_\gamma} = \frac{1}{\pi R^2} \int_{b>2R} \int_{r \leq R} n(E_\gamma, | \overline{b} - \overline{r} |) d^2r d^2b \tag{24}$$

where $n(E_\gamma, b)$ is the photon density, given by Eq. 3. This gives the cross sections and rates for $Au + Au \rightarrow Au + Au + V$ shown in Table 4. The rates are doubled to account for the

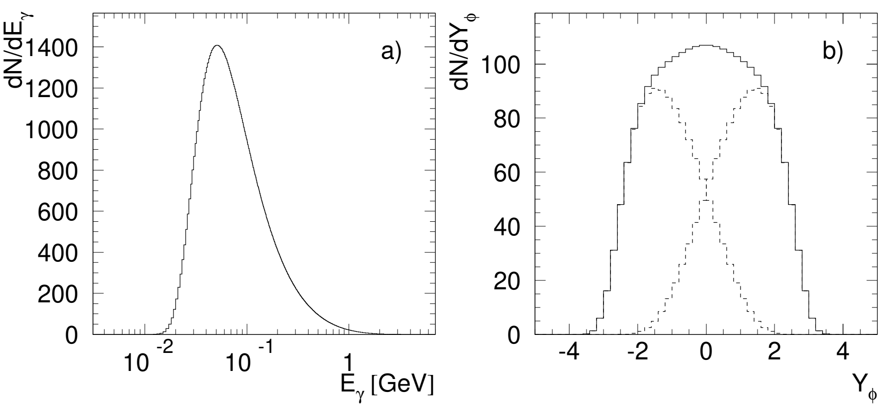

Figure 4: E$_\gamma$ and center–of–mass rapidity distribution for ϕ–meson production. The dashed histograms in b) shows the distributions when it is known which nucleus is the photon emitter and target. The asymmetry arises because the photon generally has a lower energy than the Pomeron. The solid histogram in b) shows the expected experimental distribution which is symmetric around y=0, since in an experimental situation it is unknown which nucleus is emitter or target.

photon flux from both beams. The rates for the light vector mesons are comparable or higher than for most single meson final states from two–photon interactions.

Since the Pomeron is assumed to be massless, the kinematical relations in Eq. 9 are applicable for this system as well. The momentum distribution of the final state can be obtained by taking the derivative of Eq. 23. The distribution is shown in Fig. 4, both as function of the photon energy and final state rapidity. The rapidity distribution in a given γPomeron interaction is shifted in the direction of the Pomeron (shown by the dashed histogram in Fig. 4). The total rapidity distribution is symmetric since it is arbitrary which nucleus emits the photon or the pomeron.

Since the rates in Table 4 are so high, an interesting possibility worth studying is double VM production in a single ion–ion interaction. The probability of vector meson production for a given impact parameter, $d\sigma/d^2b$, is plotted in Fig. 5. The solid curve in the figure shows the result of a numerical integration of Eq. 24, and the dashed curve shows the approximate result when the photon flux is calculated as the integration of Eq. 3 from 2R to ∞. There is a difference only at small impact parameters. For grazing nuclear collisions (b=2R), the probability of producing a ρ–meson is about 0.4%. In the absence of coherence or other correlations, for $b = 2R$, the probability for producing two ρ's is thus $(0.004)^2$.

3.3 Nuclear Breakup

One final state observable is the status of the outgoing gold nuclei. Although the momentum transfer to the nuclei from coherent interactions is far too small to be measured, it may cause the nucleus to be excited or break up. One of the simplest excitations is a single photon

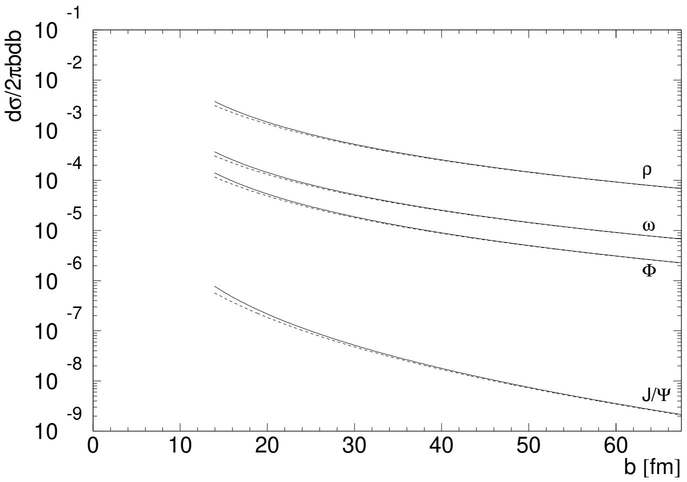

Figure 5: Probability for vector meson production, $d\sigma/d^2b$, as function of impact parameter in Au+Au interactions.

(spin 1 exchange) excitation into a giant dipole resonance (GDR). In a GDR, the protons collectively oscillate with the neutrons in the resonance. A GDR usually decays by emission of one or more neutrons, which can be detected in the STAR zero degree calorimeter.

When a two-photon interaction occurs, the two nuclei may also exchange an additional photon or photons, leading to an excitation[30]. This is the dominant source of GDR, much more likely than the possibility of one of the two directly involved photons causing an interaction. Because the time scale for breakup is long compared with the two–photon interaction, the luminosity is not affected.

At RHIC, for a grazing ($b = 2R$) gold collision, the excitation probability is about 35% per nucleus. For smaller nuclei, the probability is much lower; for calcium, it drops to 1%. This additional photon interaction may also happen for photonuclear interactions. At larger impact parameters, the probability drops rapidly. Because of this, it may eventually be possible to use nuclear breakup to tag on impact parameters, and possibly statistically separate two-photon from photonuclear interactions.

4 Rates in STAR

Here, we will consider an optimistic year 1 configuration for STAR: main TPC, 2 forward TPCs and full MWPC and CTB barrel for triggering. When they arrive, the SVT and calorimeter will expand the reach of the peripheral collisions program, but, since this memo is concentrating on year 1 physics, we do not consider them further here. When the EMC barrel is complete, it will vastly increase our capabilities by allowing the reconstruction of neutral states, improving electron identification and sharpening triggering. The Vertex Position Detector may also be useful in reducing trigger rates and backgrounds, since it covers a nonnegligible range of pseudorapidity.

The rates for observing final states in STAR depend on the production rates, geometric efficiency, triggering efficiency (discussed later) and the reconstruction efficiency. Because of problems with tracks splitting into two during reconstruction, we cannot yet calculate overall reconstruction efficiencies. Here, we will only consider events completely contained within the TPC, and tracks will be assumed to be reconstructed if they have $p_T > 150$ MeV/c and $|\eta| < 1.5$. Because the multiplicities are very low, tracks in this region of phase space should be reconstructed with very high efficiency.

With these geometric acceptance criteria, we find the acceptances for various final states given in Table 5. All rates are for gold beams. Specific analyses may use additional final state specific cuts, as will be discussed in detail in Section 7.2.

Besides tracking, many peripheral collisions analyses will require particle identification (PID). Until there is a TOF system and calorimeter (for electrons), PID will rely on dE/dx measurements in the TPC. Because, in most cases, we will be considering pairs of particles (for example, separating $\pi^+\pi^-$ from K^+K^-), separation is considerably simplified. However, PID capability will limit the range of some analyses.

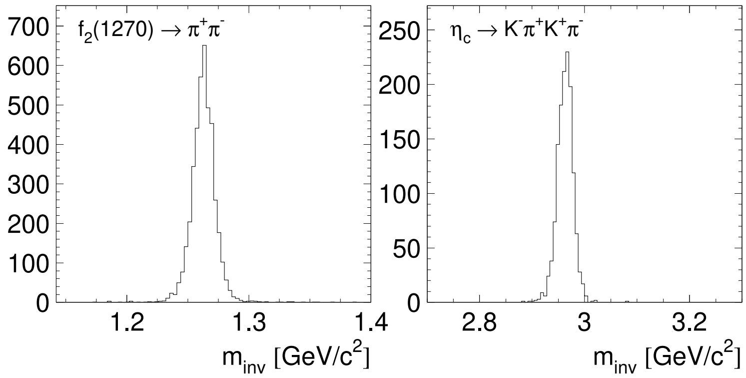

Figure 6: Reconstructed invariant mass distributions. The RMS widths are 11 MeV and 16 MeV for the $f_2(1270)$ and η_c, respectively.

We have investigated the accuracy of reconstruction by simulating $\gamma\gamma \to f_2(1270) \to \pi^+\pi^-$ and $\gamma\gamma \to \eta_c \to K^-\pi^+K^+\pi^-$ events with STARlight and GSTAR, and reconstructed them with the standard reconstruction software. In the simulations the natural width has been neglected in order to study the width due purely to the detector resolution. The reconstructed mass peaks are shown in Fig. 6. Particle identification has been assumed in these calculations. The reconstructed peaks have RMS widths of 11 MeV and 16 MeV for $f_2(1270)$ and η_c, respectively. The width for $f_2(1270)$ is considerably narrower than the natural width ($\Gamma = 185 \pm 20$ MeV), while the width for η_c is of the same order as the natural width ($\Gamma = 13 \pm 4$ MeV).

5 Backgrounds

In this section the different sources of background to two–photon interactions will be discussed. Four background processes have been identified: peripheral (hadronic) nucleus–

Final State	Prod. Rate (Evts./year)	Decay Mode	Br. Ratio (%)	Efficiency (%)	Geom Det. Rate (Evts./year)
$f_2(1270)$	1,100,000	$\pi^+\pi^-$	56.5	65	400,000
$\eta_c(2980)$	5,100	$K^-\pi^+K^+\pi^-$	2.0	36	37
$\rho^0\rho^0$	43,000	$\pi^+\pi^-\pi^+\pi^-$	100.0	23	10,000
$\mu^+\mu^-$	$2.7 \cdot 10^8$	–	–	5.0	$13 \cdot 10^6$

Table 5: Production rates (for gold on gold) and detection efficiencies for various final states. The η_c is for a single decay mode; other modes could be added in to increase the efficiency.

nucleus collisions, beam–gas interactions, photonuclear interactions, and cosmic rays. Each of these will be discussed in the following subsections. The trigger algorithms and off–line analysis cuts which have been developed to separate signal from background will be discussed in the following two sections.

5.1 Peripheral (hadronic) A+A Collisions

Hadronic gold–gold interactions at RHIC will occur at a rate of about 1.3 kHz ($\sigma_{Au+Au}^{nuclear}$ = 6500 mb). High multiplicity central Au+Au collisions should be easy to distinguish from two–photon events. At larger impact parameters, fewer nucleons participate in each interaction, and the multiplicity drops. Even though an average of 21.5 charged tracks are produced in a single pp interaction at $\sqrt{s}$=200 GeV[41], fluctuations in multiplicity and emission angles will cause some hadronic events to produce only a few tracks in the TPC, and thus resemble a two–photon interactions. The rates are best estimated with Monte Carlo simulations.

Simulations were performed with two standard Monte Carlo models: FRITIOF 7.02[42] and VENUS 4.12[43]. Both models have been shown to reproduce the production of charged particles in heavy–ion interactions at lower energies (CERN SPS). There are significant differences between the models illustrated for instance by the different predictions of nuclear stopping, K/π–ratio etc., but these differences should not be important for the background simulations presented here.

Events were generated with FRITIOF and VENUS for impact parameters in the range 12–20 fm. The range includes all events that could result in a level 0 trigger. The impact parameter distribution for events having between 2 and 5 tracks in the TPC is shown in Figure 7.

The selected impact parameter range corresponds to a geometric cross section of 8042 mb and an interaction rate of 1608 Hz. The relevant background trigger rates are obtained from the simulated events by applying the cuts developed for the trigger algorithms, as will be discussed in Section 6.

5.2 Beam-gas Interactions

Interactions between the beam–projectiles and the nuclei in the gas inside the beam pipe can occur anywhere along the beam–pipe, both inside and outside of the STAR TPC. In

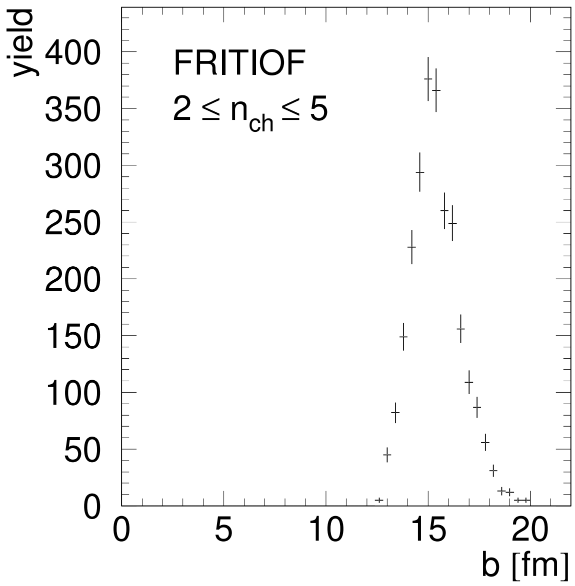

Figure 7: Distribution of impact parameters for Au+Au events producing between 2 and 5 tracks in the TPC, as given by FRITIOF.

this section only interactions inside the TPC are discussed. These are the most important, firstly because the encaps of the TPC should provide shielding against beam–gas interactions occurring outside of the TPC. Furthermore, because of the position of the vacuum pumps and the lower temperatures around the magnets, the gas pressure will be lower outside than inside of the TPC and this will reduce the number of interactions occurring there. Level 3 of the trigger will be able to find the vertex position, and hence reject most beam–gas interactions by removing interactions outside of the interaction diamond. Because of this, beam-gas interactions are a problem mainly at trigger levels 0 and 1.

The gas in the beam–pipe (warm bore) has been assumed to consist of [45]:

$$90\%\ H_2 \quad 5\%\ CO \quad 5\%\ CH_2$$

In the simulations, the carbon (A=12) and oxygen (A=16) nuclei have been treated equally as "nitrogen" (A=14).

Assuming an ideal gas at room temperature (T=293 K) and a pressure of 10^{-9} Torr, the following nuclear densities are obtained

$$\begin{aligned} \text{H} &: \; 6.60 \cdot 10^{13}\ \text{m}^{-3}, \\ \text{“N”} &: \; 4.95 \cdot 10^{12}\ \text{m}^{-3}. \end{aligned}$$

The flux of Au–nuclei is calculated from the number of particles/bunch (10^9) and the time between bunch crossings (210 nsec for the RHIC design luminosity; future upgrades may decrease this number to 105 nsec.) The beam-gas interaction rate can be estimated from the total nuclear Au+p and Au+N cross sections, 1923 mb and 2982 mb, respectively, as calculated with the Bradt–Peters formula[44]. This gives interaction rates of 0.60 $cm^{-1}s^{-1}$ for hydrogen and 0.07 $cm^{-1}s^{-1}$ for "nitrogen". Of course, only a small fraction of these will give rise to triggers similar to two–photon interactions.

To simulate beam–gas interactions, the nucleus–nucleus Monte Carlos FRITIOF and VENUS were again used. Events were generated for Au+p (impact parameters between 0 and 12 fm) and Au+N (impact parameters between 0 and 15 fm). We mention, for future use, that these impact parameter ranges correspond to geometric cross sections of 4524 mb and 7069 mb; of course in most cases there is no interaction for b =15 fermi. The cross sections are scaled downward by the probability of an interaction.

A pressure of 10^{-9} Torr is realistic for the beam–gas at the center of the TPC. Further from the detector, closer to the vacuum pumps, the pressure will be lower; we assume 10^{-10} Torr. In the simulations, the pressure has been assumed to decrease linearly from 10^{-9} Torr at the center of the TPC ($z = 0$) to 10^{-10} Torr at the edges ($|Z|$=200 cm), as illustrated in Fig. 8. With this profile, the total Bradt–Peters beam gas interaction rates for H and N are about 264 Hz and 31 Hz respectively (for both beams).

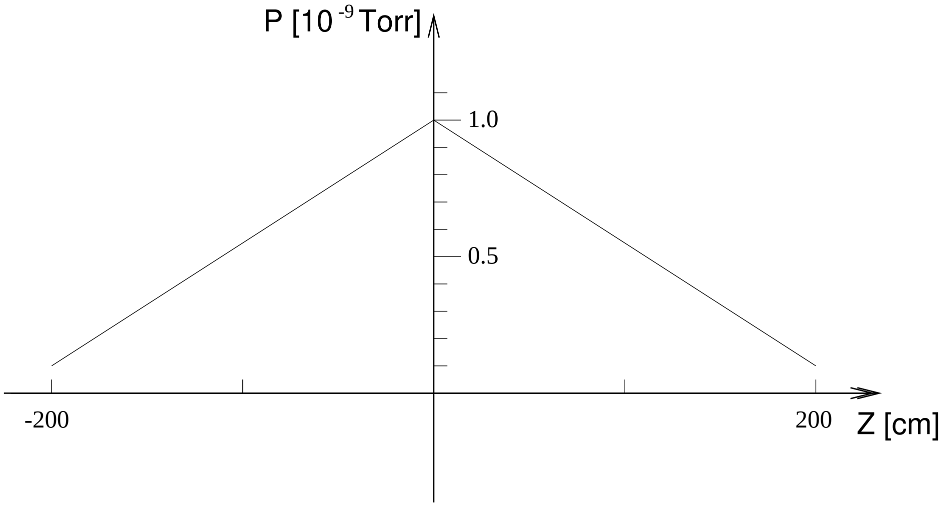

Figure 8: The beam–gas pressure profile used in the simulations.

5.3 Upstream Interactions

It is possible for gold nuclei to interact with beam gas molecules or the beampipe far upstream of STAR, producing debris which may trigger the detector. Although these events cannot mimic peripheral collisions, they may cause the detector to trigger. Alan Stevens has modeled these events; at a pressure of 10^{-9} Torr, there are about 0.6 interactions per second per cm of beampipe. Since the pressure in the cold sections of the beampipe is expected to be 10^{-10} Torr, this is a conservative estimate. For the $\sim$ 35 m of path length that can 'see' the STAR detector, there are 2100 interactions per second. Stevens considered these interactions with a simple model, simulated the breakup of gold nuclei, and tracked these particles through a model detector.

We estimate the effect on trigger rates with a simple model. These interactions can contribute to the STAR trigger if they reach the detector at a radius between 50 and 200 cm from the beampipe. In the simplest case, each track will count as two tracks from triggering, as it enters and exits the TPC. Stevens found that at 50 cm, the particle fluence per interaction was about $0.008/\mathrm{cm}^2$, while at 200 cm, it was about $0.001/\mathrm{cm}^2$[46]. Each interaction will cause an average of about 240 particles to pass through the TPC. Particles showering in the magnet poles may increase this number. So, these events are most likely to mimic medium bias triggers. Some upstream interactions may produce low multiplicity triggers, but the rates are likely to be small. If necessary, the rates can be further reduced by topological requirements on the trigger.

5.4 Photonuclear Interactions

The photon flux associated with the strong electro–magnetic fields of the interacting nuclei may, in addition to two–photon interactions, give rise to photon–nucleus interactions. In the rest frame of one of the Au–nuclei, the photon energy spectrum extends up to $E_\gamma = \gamma\hbar c/R \approx 330$ GeV. This energy is sufficient for significant particle production.

The Weizsäcker–Williams method has again been used to calculate the photon flux hitting a nucleus. This calculation is performed in the rest frame of one of the nuclei. The photon spectrum is calculated from:

$$E_\gamma \frac{dN}{dE_\gamma} = \frac{2Z^2\alpha}{\pi}\left\{xK_0(x)K_1(x) - \frac{1}{2}x^2\left(K_1^2(x) - K_0^2(x)\right)\right\} \quad (25)$$

where $x = E_\gamma b_{min}/\beta\gamma$, E_γ is the photon energy, and $b_{min} = 2R$. This distribution is shown in Fig. 9. The total interaction rate is:

$$2 \ \mathcal{L} \ \sigma_{\gamma+Au} \ \int_{E_{min}}^{\infty} \frac{dN}{dE_\gamma} dE_\gamma \quad (26)$$

where the factor 2 comes from the two beams. For the cross section $\sigma_{\gamma+Au}$ a value of 14.4 mb was used[47].

Photonuclear interactions were simulated with the Monte–Carlo model DTUNUC [47], one of the few codes available to simulate high energy photonuclear interactions. Because of the $1/E_\gamma$ dependence of the photon energy spectrum it is necessary to introduce a low–energy cut–off. Since the model DTUNUC is not designed to handle photon energies below $\sim$5–10 GeV, we used E_{min}=10 GeV. The right part of Figure 9 shows the photon energy distribution for events with between 2 and 5 tracks in the TPC. The distribution is zero below 10 GeV showing that the 10 GeV cut–off does not miss background events.

Eq. 26, integrated from $E_{min} = 10$ GeV, gives a total photonuclear rate of 864 Hz. The actual trigger rates are obtained by applying the trigger cuts to the simulated events.

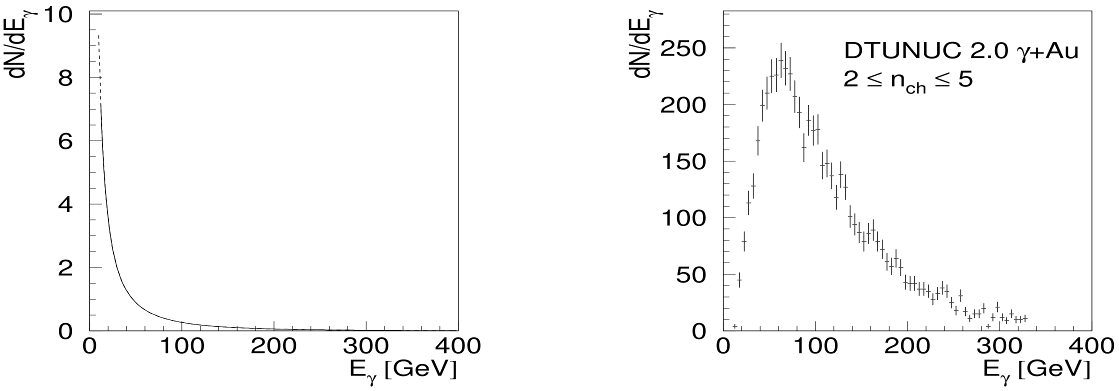

Figure 9: Left: Weizsäcker–Williams photon energy distribution. Right: Photon energy distribution for events with TPC multiplicity between 2 and 5.

5.5 Cosmic Rays

The total flux of cosmic rays crossing a unit horizontal area from above is[4]:

$$1.8 \cdot 10^2 \text{ m}^{-2} \text{ s}^{-1}$$

Treating the TPC as a rectangle with area 16.0 m^2 $(2 \cdot r \cdot l)$ gives a rate of cosmic rays entering the TPC of 2880 Hz.

Cosmic rays were simulated with the Monte-Carlo HemiCosm[48], developed by the BaBar collaboration. HemiCosm generates cosmic ray tracks (muons) according to parameterizations of experimental energy and angular distributions. A low–energy cut–off of 1 GeV muon energy is implicit in the model. The calculations account for the TPC geometry and the fact that only muons with $E > 1$ GeV are included. The net effect is a HemiCosm total rate of 2820 Hz, very similar to what is obtained for a rectangle of area 16 m^2.

The distributions of cosmic ray flight times through the STAR TPC is shown in Figure 10. The path length for a vertical cosmic ray is 4 m, corresponding to a flight time of 13.3 nsec. This is the most probable flight time, as can be seen in the figure.

The simulations show that 48% of the cosmic rays both enter and exit the TPC through the Central Trigger Barrel. The rest exit or enter through the endcaps. These simulations do not (yet) consider the fact that a nearly vertical cosmic ray entering or exiting the TPC through the endcaps is likely to hit many MWPC wires, and thus not cause a trigger.

Shielding by the roof and walls of the building, the magnet steel etc. are not included in the present simulation. Our best estimate is that the shielding will reduce the rates by about 20%. For these reasons, these rates are very conservative.

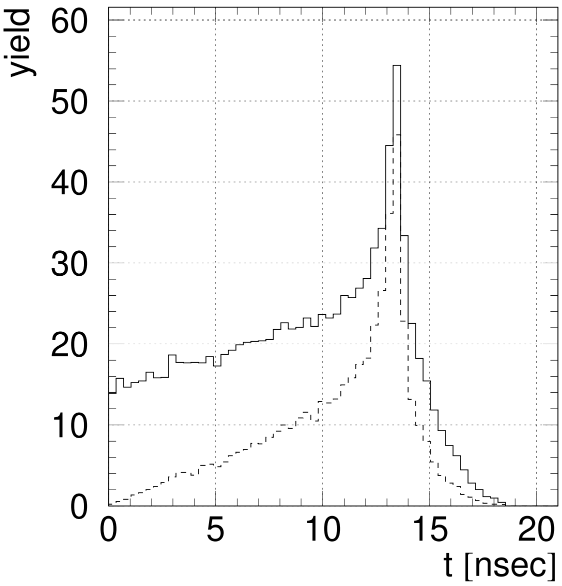

Figure 10: Distribution of cosmic ray flight times through the STAR TPC as predicted by HemiCosm. The dashed histogram shows the distribution for tracks which both enter and exit through the Central Trigger Barrel (CTB).

6 Triggering

The two main trigger detectors used here are the Central Trigger Barrel (CTB) and Multi–Wire Chambers (MWC) at the endcaps of the TPC. At the highest trigger level, some tracking information from the TPC will also be available for triggering.

The 240 plastic scintillator CTB slats surrounding the TPC cover the pseudorapidity interval $|\ \eta\ | < 1.0$. The MWC, its wires being identical to the TPC anode wires, will measure the charged particle multiplicity in the interval $1.0 < |\ \eta\ | < 2.0$.

The STAR trigger is divided into 4 levels, as shown in Table 6. Levels 1 and 2 are combined here because it is not clear what calculations are possible in Level 1 and what will have to wait until level 2. The raw data from the CTB and the MWC will be available and can be processed by the FPGA based level 0 in about 1 μs. In levels 1 and 2, the same information can be studied in a computer, producing more accurate multiplicity information by merging adjacent hits. Real TPC tracking will be available in level 3, after approximately 10 ms. The specific trigger algorithms for each level will be discussed more accurately below.

Level 0: At level 0 the multiplicity in the pseudorapidity interval $|\ \eta\ | < 2.0$ can be estimated from the CTB and MWC data. Here, a cut was applied requiring the number of tracks in the TPC to be between 2 and 5. Multiplicities 3 and 5 are kept at this level since single hits giving rise to signals on multiple wires in the MWC are not properly merged.

Trigger Level	Decision Time	Detectors
0	$\sim 1\ \mu$s	CTB,MWC
1/2	$\sim 100\ \mu$s	CTB,MWC
3	~ 10 ms	TPC

Table 6: A summary of the trigger levels and the corresponding decision times in STAR.

The information from the CTB and MWC can be divided into four bins in azimuthal angle at level 0. The angular information is used to apply cuts on the general topology of the events. The very low value of the summed p_T in two–photon interactions gives the reaction products a symmetry in azimuthal angle. In case of a 2-particle meson decay, the daughter tracks will emerge almost back–to–back in the transverse plane.

Topology cuts were applied to the different event multiplicities. For 2 track events, the two tracks were required to be in opposite sectors. Events with 3 observed tracks were assumed to in reality correspond to 2 track events with one split hit. The topology cut for 3 track events is therefore that 2 of the tracks be in the opposite sector to the third. For 4 and 5 track events, no half circle in ϕ can be empty.

Without additional requirements, the largest background at level 0 appears to be cosmic ray muons. Most of these muons can be rejected by using timing information from the CTB slats in level 0 of the trigger. Particles produced by in-time interactions in the interaction diamond will produce CTB output within a fairly well defined ~ 10 nsec time window out of the 105 nsec beam crossing interval, as shown in the figure below, while cosmic rays are randomly spread in time. Since a relativistic muon takes ~ 13.3 nsec to cross the center of the TPC, the probability for both the incoming and outgoing cosmic ray CTB hits to be in this narrow time window is very low. So, cosmic ray trigger rate can be reduced by limiting the CTB acceptance time window shown below.

The size of the window and its offset from 0 must of course be tuned so that as little real data as possible is lost. The rate of cosmic ray level 0 trigger as the size of the time window is varied from 5 nsec to 40 nsec is shown in Figure 11.

Level 1/2: At level 1/2 improved CTB and MWC multiplicity information is available. The multiplicity cuts are thus sharpened to n_{ch}=2 or n_{ch}=4. Furthermore, it is required that all tracks are within $\mid \eta \mid \leq 1.5$, and that the region $1.5 <\mid \eta \mid < 2.0$ is empty. The latter cut will have a small effect on the acceptance, since tracks in this region have a poor momentum resolution.

No distinction between trigger levels 1 and 2 have been made in this analysis. It is still unclear when the electromagnetic calorimeter will be complete and contribute to the trigger; this may be a significant help at levels 0 and 2.

Level 3: At level 3 tracking information from the TPC will be available. This will enable cuts to be applied on the momenta of the particles and, as will be shown, this can reduce the

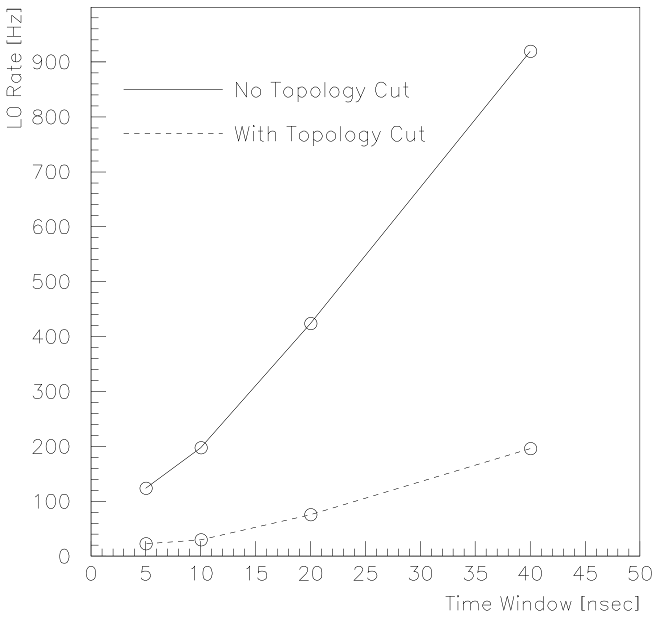

Figure 11: Rates of cosmic ray level 0 triggers as function of the size of the CTB time window. The rates have been calculated for a bunch crossing period of 105 nsec.

number of background interactions considerably. Furthermore, the particle charge can be determined from the curvature of the tracks. It is thus possible to reject background events which have $\sum Q_i \neq 0$. Finally, the primary vertex can be located, and beam-gas and cosmic ray interactions outside the interaction diamond rejected.

The cuts used for the trigger simulations in this analysis were: $\mid \sum p_T \mid \leq 100$ MeV/c, $\sum Q_i = 0$, and $\mid Z_{vertex} \mid \leq 20$ cm. For cosmic rays, a cut on the minimum perpendicular distance from the beam of 2.0 cm was also applied.

Trigger Level	Hadronic A+A FRITIOF	VENUS	Beam–Gas FRITIOF	VENUS	γ+A DTUNUC	Cosmic Rays HemiCosm	Total Rate
0	18	21	53	53	63	26	160
1/2	2	4	6	7	11	18	38
3	0.03	0.1	0.1	0.1	0.6	0.4	1.2

Table 7: Trigger Rates (in Hz) of the various background processes discussed in the text for gold–beams at the design luminosity. A CTB timing window of 10 nsec is assumed.

The resulting trigger rates are shown in Table 7. These rates are rather conservative. The cosmic ray muon rates are too high for the reasons discussed earlier. A collinearity cut at level 3 could reduce the cosmic ray rate to almost zero. Finally, the topological cuts possible at levels 0 and 1 need to be optimized. It may also be possible to use information from the ZDC and VPD (when available) to reduce the trigger rates without losing useful events. We are developing trigger algorithms so that, at each level of the trigger pipeline, peripheral collisions will use only a small fraction of the available bandwidth (rate), so that peripheral collisions will have only a small impact on the central collisions program.

The rates in the table can be compared to the rate of triggers from coherent photonuclear $\rho^0 \rightarrow \pi^+\pi^-$ production, 10 Hz, or to the rate of μ–pairs from two–photon interactions, 1.3 Hz. As the RHIC luminosity rises toward the design goal, a significant fraction of our effort in the trigger will be devoted toward rejecting these interesting low mass photonuclear and two–photon events – another demonstration that todays signal is tomorrows background. This rejection can be implemented by tighter topological cuts to eliminate events where curvature in the STAR magnetic field bends the tracks significantly, so they are no longer back to back.

7 Off–line Analysis

7.1 General Techniques

Off–line, improved TPC tracking information will be available as will additional information from the other STAR detectors. This data will be used to improve the background rejection over the trigger level. Here, the only additional STAR components considered are the forward TPCs. In this section the general techniques for off–line analyses will be discussed, while the specific sample analyses will be discussed in Section 7.2.

Since it is assumed that the entire final state in a coherent peripheral event will be observed in the main TPC, events with any tracks in the FTPCs can be removed. Here, a simple model of the FTPC acceptance is used: $2.5 \leq\mid \eta \mid\leq 3.75$ and $p_T > 100$ MeV/c.

Although most events occurring outside the interaction diamond will be rejected by the trigger level 3, offline, improved tracking and knowledge of the diamond position should make it possible to sharpen these cuts. This will be most effective in removing cosmic ray tracks which pass at a non–zero perpendicular distance from the beam–line. This should reduce cosmic ray backgrounds to negligible levels; they are not considered further here.

Coherent collisions are characterized by a low total transverse momentum. Offline, the cut on p_T can be sharpened from that used in the trigger. In a coherent event the maximum p_T is given by $\sqrt{2}\hbar c/R \sim 45$ MeV/c for Au+Au. Here, a cut of $\sum p_T \leq 50$ MeV/c is used.

Since the cut on $\sum p_T$ is of central importance to the background rejection, the effects of the detector resolution on $\sum p_T$ have to be understood. The resolution has been studied through GEANT(gstar) simulations, as was discussed in Section 4. Figure 12 shows the $\sum p_T$ distribution for $\gamma\gamma \rightarrow$ f$_2$(1270)$\rightarrow \pi\pi$ together with the distribution for the background processes. The production and decay of the $f_2(1270)$ have been simulated with STARLight, and the events have been run through gstar and the STAR reconstruction chain. As can be seen, the detector resolution has a relatively minor effect on $\sum p_T$. A cut of 50 MeV/c does

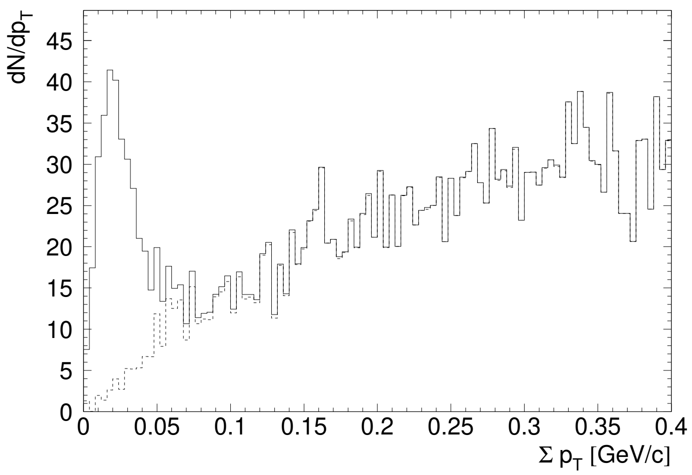

Figure 12: Summed p_T for two–photon signal $\gamma\gamma \rightarrow$ f$_2$(1270)$\rightarrow$ $\pi\pi$ and backgrounds. The statistics corresponds to approximately 72 hours of Au+Au running at the RHIC design luminosity. (The solid histogram shows the signal plus background, and the dashed histogram shows the background.)

not significantly reduce the signal.

The kinematics of two major background sources, beam–gas and photonuclear events, are very different from the kinematics of a two–photon event. The difference can be seen in the final state center–of–mass rapidity. As Fig. 13 shows, the distribution of Y_{CM} for two–photon events is peaked at 0, as is the case for hadronic nucleus-nucleus collisions. For beam–gas interactions (fixed target) and photonuclear interactions (dominated by low–energy photons because of the $1/E_\gamma$ dependence of the photon flux) the distribution has a clear dip in the middle. The contribution from the latter processes can thus be reduced by restricting the maximum allowed $\mid y_{cm} \mid$. Here, $|y_{cm}| \leq 0.75$ was used.

Particle identification has not yet been studied in detail. For more exotic final states, such as $\eta_c \rightarrow K^+\pi^-K^-\pi^+$, it may be necessary.

Reaction	Model	Generated Events	Events in Subsample	Rejection Factors FTPC	$\sum p_T$	y_{cm}
A+A	FRITIOF	2,714,063	2,734	0.069	0.0055	0.595
	VENUS	1,533,364	2,072	0.319	0.0097	0.736
Beam–gas	FRITIOF	190,151	4,568	0.107	0.0105	0.372
	VENUS	263,193	5,460	0.169	0.0156	0.404
γ+A	DTUNUC	190,000	5,642	0.376	0.0059	0.458

Table 8: Summary of the effects of off–line cuts for 2–track events. The values for beam–gas represent Au+p interactions.

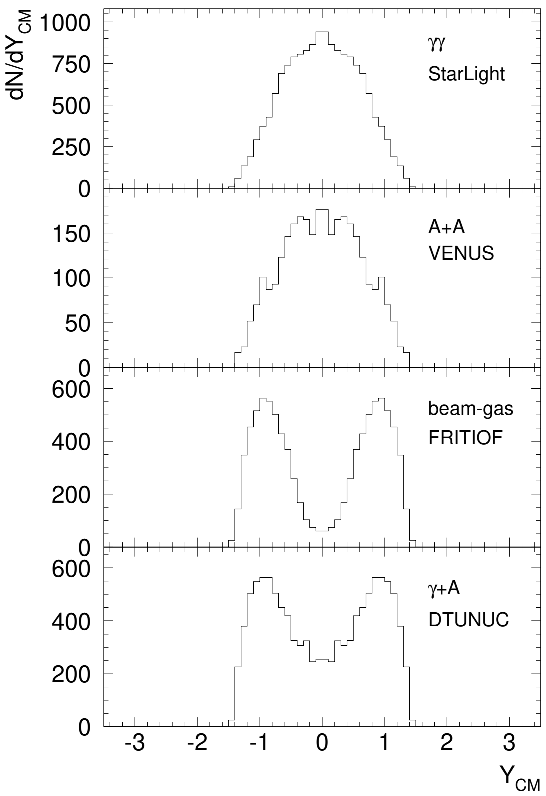

Figure 13: Center–of–mass rapidity distribution for $\gamma\gamma$–events compared with the corresponding distributions for the different background processes. The distributions have been calculated as the CM rapidity of the charged particles within the TPC acceptance, i.e. $\mid \eta \mid$<1.5 and p_T >150 MeV/c.

The off–line analysis cuts are very efficient in rejecting background interactions. To prevent the background samples from running out of statistics it is necessary to use some extrapolations to determine the final background rates. For this, two subsamples of events, one having 2 and the other 4 charged tracks within the TPC acceptance, have been generated. For both samples, we required $\sum Q_i = 0$. The final off-line cuts have then been applied on the events in the subsample, one at a time, and the cut efficiencies multiplied together.

The total number of events generated, the number of events in each sub–sample, and the rejection factors for the FTPC, P_T and y_{cm} cut are summarized in Tables 8 and 9. The rejection factors are the reduction in background when a particular cut is applied to one of the samples. For example, for beam–gas events simulated by VENUS, requiring the FTPC to be empty removes 83.1% of the 2–track events.

Reaction	Model	Generated Events	Events in Subsample	Rejection Factors FTPC	$\sum p_T$	y_{cm}
A+A	FRITIOF	2,714,063	2,082	0.052	0.0014	0.859
	VENUS	1,533,364	1,281	0.194	0.0031	0.895
Beam–gas	FRITIOF	2,474,411	1,048	0.113	0.0124	0.109
	VENUS	2,507,805	1,190	0.208	0.0042	0.162
γ+A	DTUNUC	790,000	2,058	0.236	0.0044	0.566

Table 9: Summary of the effects of off–line cuts for 4–track events. The values for beam–gas represent Au+p interactions.

7.2 Sample Analyses

This section will discuss several sample analyses and estimate the background rates for the final states discussed in Chapter 4. The μ–pairs production rate will be so high that a signal should be detectable already at the trigger level. Muons will therefore not be further discussed in this section. However, the muons themselves can be seen as a background to final states consisting of two pions or two muons.

For the other systems, estimates of the total background after all analysis cuts have been applied will be calculated. The basis for the calculations is the information in Tables 8 and 9. Knowing the cross sections and corresponding rates for the generated samples, the rate for each subsample (2 or 4 track events) can be calculated. (The cross sections for the generated samples are given in Chapter 5.) The final background rates are then found by applying the rejection factors to this rate. The resulting rates for one year of running (10^7 s) are shown in Table 10.

	System $f_2(1270)$	$\rho^0\rho^0$	$\eta_c(2980)$
Within STAR Acceptance	400,000	10,000	37
After analysis cuts	310,000	8,900	34
Peripheral AA (FRITIOF/VENUS)	400/4,000	50/460	90/680
Beam–gas (FRITIOF/VENUS)	400/1,000	6/6	<1/<1
γ+A (DTUNUC)	15,000	1,000	730
Background w/o PID	16,000/20,000	1,000/1,500	820/1,400
Background w PID			9/15

Table 10: Estimated signal and background rates (Events/year) with and without particle identification, for production of $f_2(1270)$, $\rho^0\rho^0$ and $\eta_c(2980)$ in Au+Au collisions.

In addition to the rejections in Tables 8 and 9, cuts have also been applied to the invariant mass distributions in order to arrive at the final rates. For the $f_2(1270)$, $\mid m_{\pi\pi} - m_{f_2} \mid \leq \Gamma$, where Γ is the natural width (Γ = 185 MeV); for ρ–pairs, $1.5 \leq m_{inv} \leq 1.6$ GeV/c^2; and for the $\eta_c(2980)$, $\mid m_{inv} - m_\eta \mid \leq 40$ MeV. The limit for $\eta_c(2980)$ was taken as $\pm 2\sigma$ were σ is the expected observed width, calculated from $\sim \sqrt{\Gamma^2 + (\Delta m_{inv})^2}$ where Γ is the natural width (13 MeV) and Δm_{inv} is the resolution in invariant mass ($\sim$16 MeV, cf. Fig. 6). For the $f_2(1270)$ and $\rho^0\rho^0$ all tracks are assumed to come from pions in the calculation of the invariant mass. For the η_c, the invariant mass is calculated for the four possible $K^+\pi^-/K^-\pi^+$ combinations of the 2 positive and 2 negative tracks.

For the $f_2(1270)$, photonuclear interactions are the dominant background. For the $\rho^0\rho^0$ and η_c, the photonuclear rate is still largest, but VENUS predicts that the peripheral AA contribution is very significant. FRITIOF gives AA rates about a factor of 10 lower.

For the $f_2(1270)$ and $\rho^0\rho^0$ good signal to background ratios are obtained. For the $\eta_c(2980)$ the situation is a little bit worse. Further background suppression for $\eta_c(2980)$ can be achieved with particle identification. The $\eta_c(2980)$ decays to 2 π's and 2 K's. With particle identification, the backgrounds could be reduced by 95–97%, to total rates of 9 (FRITIOF) or 15 (VENUS) events/year, small enough that the η_c should be visible. For more realistic estimates, a detailed dE/dx simulation is required. With good PID it could thus be possible to see also a $\eta_c(2980)$ signal from two–photon reactions.

The differences between the FRITIOF and VENUS predictions are large, especially for peripheral nucleus–nucleus collisions. The most striking difference is the effect of the FTPC cut. Whereas in FRITIOF this cut removes 93% of the 2–track events, in VENUS only 68% of the events are rejected. This difference thus corresponds to a factor of 5 higher final rates for VENUS. Also the cut in p_T has different effects in the two models, although here the statistical errors are larger since so few events survive this cut. For two–track events, 0.5$\pm$0.1% (stat. error) of the events in FRITIOF survive, while for VENUS the corresponding number is 1.0$\pm$0.2%. This difference results in an additional factor of 2 difference in the final rates. For beam–gas events the differences are smaller, resulting in a final rate difference of "only" a factor of 2 for $f_2(1270)$. Since we cannot tell which of the two models is more reliable in this context, we treat the differences as an estimate of the systematical errors for the background estimates.

The backgrounds shown in Table 10 are preliminary. They are examples of what is possible with a given set of cuts. If, for instance, beam–gas or photonuclear events turn out to be a more serious problem than the present estimates indicate, a stricter cut on y_{cm} could be applied. Although such a cut would reduce the total signal, it would significantly improve the signal to background ratio.

8 Other Peripheral Collisions Topics

All of the topics discussed so far involve interactions of fields coupling coherently to the entire nucleus. However, there are a number of interesting peripheral collision topics that do not involve this coherent coupling. Although they are not year 1 analyses, they may be possible once the entire electromagnetic calorimeter barrel is installed.

8.1 Photon–Gluon Interactions

Photon-gluon interactions can be a significant source of open charm in peripheral collisions[49]. Since the photon spectrum is known, these interactions can be used to study the gluon structure function.

These events would be characterized by two D mesons, probably detected by their semileptonic decays, with little else in the event. Unlike the coherent interactions, $p_\perp$ can be large. Although the rates for these interactions are large, the backgrounds have yet to be studied.

8.2 Gluon–Gluon Interactions at Large Radii

It seems likely that the EMC effect comes about because nucleon structure functions vary depending on their surrounding environment. If this is the case, then the nucleon structure function should depend on the nucleons position inside the a heavy nucleus; nucleons at the center of the nucleus should exhibit a greater change, while those at the nuclear surface should be much less affected. By studying charm production, Drell-Yan dileptons and J/ψ production in large impact parameter collisions (for example, with $b > 1.8R$), the structure functions can be studied in the nuclear surface[50]

9 Conclusions

We have presented a wide variety of physics topics that can be studied with coherent peripheral collisions at STAR. We have also discussed their feasibility, through judicious use of sample analyses. Although much work remains to be done, at this point we have a good understanding of the initial physics goals, signal and background rates, and trigger and analysis techniques required to study peripheral collisions with STAR.

For two–photon interactions, production rates of well established mesons in the mass range 1–2 GeV will be high, and we have shown that signals can be separated from backgrounds with a good signal to background ratio. The same is true for meson pairs ($\rho\rho$). With particle identification also heavier mesons (e.g. η_c) can be studied. The backgrounds to photonuclear events have not been studied in detail yet, but since the production rates are high and the kinematics is similar to the two–photon case, we expect the signal to background ratios to be high.

References

[1] *Conceptual Design of the Relativistic Heavy Ion Collider*, BNL–52195, May 1989, Brookhaven National Laboratory.

[2] Klein, S. and Scannapieco, E., STAR Note 243, Feb. 1995 (unpublished).

[3] Godand, R. *et al.*, Phys. Rev. Lett. **79**, 3829 (1997).

[4] Barnett, R. M. *et al.*(PDG), Phys. Rev. **D54**, 1, mini-review on pg. 558.

[5] Achasov, N. N., and Shestakov, G. N., Sov. Phys. Usp. **34**, 471 (1991).

[6] FELIX proposal, Lippman, E. *et al.*, CERN/LHCC 97-45, August, 1997.

[7] S. Brodsky, presentation at the Jan., 1998 STAR collaboration meeting, in the working group on peripheral collisions.

[8] Morgan, D., Pennington, M. R., and Whalley, M. R., J. Phys. G **20**, A1 (1994).

[9] Anselmino, M. *et al.*, Rev. Mod. Phys. **65**, 1199 (1993).

[10] Anselmino, M. *et al.*, Int. J. Mod. Phys. **A4**, 5213 (1989).

[11] Guclu, M. C. *et al.*, nucl-th/94110044; M. Bottcher and M. R. Strayer, Nucl. Phys. **A544**, 255c (1994).

[12] Baltz, A. J. and McLerran, L., nucl-th/9804042; Baltz, A. J., Phys. Rev. Lett. **78**, 1231 (1997).

[13] Baur, G., Phys. Rev. **D41**, 3535 (1990).

[14] Acciarri, M. *et al.*(L3 Collaboration), Phys. Lett. **B407**, 341 (1997); Akers, R. *et al.*(OPAL Collaboration), Z. Phys **C60**, 593 (1993).

[15] Forshaw, J. R. and Ross, D. A., *Quantum Chromodynamics and the Pomeron*, Cambridge University Press, 1997.

[16] Cartiglia, N, "Diffraction at HERA," hep-ph/9703245, Mar., 1997.

[17] Schellman, H., presented at the 29th Rencontres de Moriond: QCD and High Energy Hadronic Interactions, Meribel les Allues, France, 1994. Fermilab-Conf-94-219, and published in the proceedings.

[18] Ashman, J. *et al.*, Z. Phys. **C39**, 169 (1988).

[19] Müller, B and Schramm, A. J., Nucl. Phys. **A523**, 677 (1991).

[20] Schramm, A. J. and Reeves, D. H., Phys. Rev. **D55**, 7312 (1997).

[21] Cavasinni, V *et al.*, Z. Phys. C **28**, 487 (1985).

[22] Alvensleben, H., Nucl. Phys. **B25**, 342 (1971).

[23] Bartalucci, S., Nuovo Cimento **44A**, 587 (1978).

[24] Gonin, M. *et al.*, Print 97-208, presented at the 3rd Intl. Conf. on Physics and Astrophysics of the Quark Gluon Plasma, Jaipur, India, Mar 17-21, 1997.

[25] Koch, V., presented at the Jan, 1998 STAR collaboration meeting Working Group on Peripheral Collisions.

[26] Asakawa, M., Minakata, H. and Muller, B., "Non-center heavy-ion collisions are the place to look for DCC", preprint nucl-th/9802006, Feb., 1998.

[27] Scannapieco, E., private communication.

[28] Cahn, R.N. and Jackson, J.D., Phys. Rev. **D42**, 3690 (1990).

[29] Baur, G. and Ferreira Filho, L.G., Nucl. Phys. **A518**, 786 (1990).

[30] Hencken, K., Trautmann, D., and Baur, G., Z. Phys. **C68**, 473 (1995).

[31] Jackson, J.D., *Classical Electrodynamics*, New York: John Wiley & Sons, 1975.

[32] Berger, Ch. and Wagner, W., Phys. Rep. **146**, 1 (1987).

[33] F. Low, Phys. Rev. **120**, 582 (1960).

[34] F.C. Erné, in *Proc. ECFA Workshop on LEP200*, Aachen, 29 Sept.–1. Oct., 1986, Vol. I, Eds. A. Böhm and W. Hoogland (CERN, Geneva), p. 211.

[35] Budnev, V.M., Ginzburg, I.F., Meledin, V.G., and Serbo, V.G. Phys Rep. **15**, 181 (1975).

[36] Greiner, W. and Reinhardt, J., *Quantum Electrodynamics*, Springer–Verlag, 1994.

[37] Berger, C. et al., *Z. Phys.* **C38**, 521 (1988).

[38] Breitweg, J. et al., Eur. Phys. J. **C2**, 247 (1998).

[39] Crittenden, J.A., *Exclusive Production of Neutral Vector Mesons at the Electron–Proton Collider HERA*, Springer–Verlag, 1997.

[40] Drees, M., Ellis, J., and Zeppenfeld, D., *Phys. Lett.* **B223**, 454 (1989).

[41] Alner, G.J. et al. *Phys. Lett.* **B167**, 476 (1986); Ansorge et al. *Z. Phys.* **C43**, 357 (1989).

[42] Pi, H., *Comp. Phys. Comm.* **71**, 173 (1992).

[43] Werner, K., *Phys. Rep.* **232**, 87 (1993).

[44] Bradt, H.L. and Peters, B., *Phys. Rev.* **77**, 54 (1950).

[45] Kirk, P. N. *et al.*, in *Workshop on Machine Backgrounds at RHIC*, July 19-20, 1995, ed. S. White and G. Young.

[46] Stevens, Alan J., RHIC Detector Note 22, Sept., 1996.

[47] Engel, R., Ranft, J., and Roesler, S., *Phys. Rev.* **D55**, 6957 (1997); *ibid.* **D57**, 2889 (1998).

[48] Bringle, M.P., BaBar Note 163 (1994) (unpublished).

[49] Emel'yanov V., Khodinov, A. and Strikhanov, M. preprint MEPhI 026-95, 1995.

[50] Emel'yanov, V., Khodinov, A., Klein, S.R. and Vogt, R., Phys. Rev. **C56**, 2726 (1997); Emel'yanov, V., Khodinov, A., Klein, S.R. and Vogt, R., nucl-th/9805027.